Spectroscopic Identification of Galaxies in the HUDF using MUSE

Hylke Hoogland

Kapteyn Astronomical Institute, Rijksuniversiteit Groningen

June 24, 2016

Abstract

The Hubble Ultra-Deep Field (HUDF) is the field of the sky with the deepest multi-wavelength data available to date, which makes it very useful for high redshift galaxy studies. In this thesis we will analyze data taken with the new Multi-Unit Spectroscopic Explorer (MUSE) on the Very Large Telescope (VLT) of the central 1 square arcminute of this field. With a total exposure time of 5 hours and 50 minutes, we found 117 sources in the field. We found 19 intensively star forming and 4 'red and dead' galaxies out of a total of 36 objects at low redshift (z<1). The remaining objects do form stars but at a much lower rate; they have only weak emission lines in their spectra. Additionally we found 14 star forming galaxies in the range 1<z<3. For the 9 objects in the range 1.5<z<2.9, we can not say whether they are star forming or not, because no prominent emission lines can be detected by MUSE. We also found 12 Lyα emitters, although the line identification is not certain for some of these objects. Among these are 3 objects which may be a galaxy group candidate at z=5.4. For 35 objects we calculated a lower limit for the Star Formation Rate (SFR), using the luminosities of the OII and Hα emission lines. We found SFR in the range from 0.01 to 3 $M_{\odot}yr^{-1}$. We cross-matched our sources with the public CANDELS GOODS-South galaxy catalogue. This revealed that 6 objects found in our MUSE data are not present in the CANDELS catalog. Possible explanations are the low average continuum flux of line emitters and source confusion in crowded areas.

1 Introduction

Although the concept of integral field spectroscopy is not new, the Multi-Unit Spectroscopic Explorer (MUSE) provides a great leap forward in the application of this technique. Unlike other integral field spectrographs, MUSE can cover an area of one square arcminute in one pointing. With MUSE, there is no need to know the exact position of objects. This makes the instrument ideal for finding unknown objects (see also Bacon et al. 2015; Contini et al. 2015; Karman et al. 2015; Kelz et al. 2015). Even though Adaptive Optics will only be available for MUSE this summer, the resolution of the images produced is already about 0.6 to 1 arcsecond. MUSE operates in the optical and near-infrared wavelength range, from 4750 to 9350Å (Bacon et al. 2014).

The Hubble Ultra-Deep Field (HUDF) benefits from the deepest Hubble Space Telescope (HST) images ever taken of the universe. It is therefore an important source of data for high redshift studies (see also Bouwens et al. 2004; Bunker et al. 2004). In 2009, new Wide Field Camera 3 infrared (WFC3/IR) data increased the limiting magnitude of the HUDF observations to 28.5 ABmag in the Y, J and H bands (Bouwens et al. 2010). In 2012, again new WFC3/IR and F105W data were added. This new data greatly improved the visibility of high redshift (z>8.5) objects in the field (Ellis et al. 2012). Many sources in this field have been identified and studied, which makes comparing other data with the data found in this thesis easier.

The Cosmic Assembly Near-infrared Deep Extragalactic Legacy Survey (CANDELS) is a survey of five different fields in the sky, designed to study the high redshift universe (Grogin et al. 2011). The data was collected using the HST WFC3/IR channel, the WFC3 ultraviolet/optical and the Advanced Camera for Surveys (ACS) (Koekemoer et al. 2011). The Great Observatories Origins Deep Survey (GOODS) is a deep infrared survey covering two fields in the sky, one northern (GOODS-N) and one southern (GOODS-S) (Fosbury et

*s2506734@student.rug.nl; hoogland@kapteyn.astro.rug.nl

al. 2001). The CANDELS survey includes these two fields. GOODS-S covers a large area which contains the HUDF. We will compare the data from MUSE with data from this catalog.

The lay-out of this Bachelor thesis is as follows. In section 2 we discuss the observations and the data-reduction process. We present the results and analyze them in section 3. The discussion in section 4 covers the quality of the data. We present our conclusion in section 5, references in section 6 and acknowledgments in section 7. The appendix shows two tables with all the spectral properties of our sources.

2 Observations

The observations were taken at the VLT site in Chile on six nights between September 26 2014 and December 22 2014. The target is a one square arcminute field near the center of the HUDF. A total of 14 exposures of the field were made, with a total exposure time of 5 hours and 50 minutes. The instrument was rotated 90 degrees between each observation. This ensures that objects will be detected by different channels on the MUSE CCDs. MUSE utilizes 24 different channels to cover the entire field of view.

2.1 Data reduction

For a detailed description the performance of the MUSE instrument and the data reduction, we refer the reader to the papers by Bacon et al. from 2015 and 2014 and the MUSE pipeline user manual.

For every exposure, 10 or 11 bias frames were taken. The calibration frames were taken the same night as the corresponding science or standard star frames. The first observation of standard stars was done the night after the first observation of the science frame. Hence we did the data reduction steps seven times. All bias frames of one night were combined for each night to create a master bias frame of that night.

Ideally the dark frames should have been combined next, but since the dark current of the MUSE CCDs is very small, we skipped this step. We consequently performed a flat-field correction. The flat-field correction includes tracing the position of the slices on the CCDs. Each channel of the MUSE instrument contains 48 slices to record the spectra. We corrected for bad pixels in this step as well.

In order to know which pixel corresponds to which wavelength, we did a wavelength calibration. A light source with known spectrum is recorded on the instrument. The MUSE wavelength calibration detects the lines from this spectrum and assigns the wavelengths given as input to these lines. The tracing solution from the previous step is needed for this. Ne, Xe and HgCd lamps are used for calibration.

Next we performed the twilight skyflat correction which also assigns coordinates to the pixels using geometry tables. All corrections from the previous steps are applied to the twilight skyflats. We also corrected for vignetting.

Having done these steps, we applied the corrections to the science and standard star frames. Additionally a correction for the relative illumination of slices was performed. This step creates the pixel tables used for final combination of the data and an image of the science frame as it appears on the slices of the MUSE CCDs.

We compared the pixel tables for standard stars to the known flux of these stars. The fluxes are then scaled to fit and extrapolated over the entire wavelength range. We calibrated the science frame fluxes with these standard star fluxes.

Post-processing the data creates the final images and datacubes of the science frames. It includes creating a sky spectrum from the darkest parts of the data, correcting for the radial velocity of the observer and applying an astrometric solution.

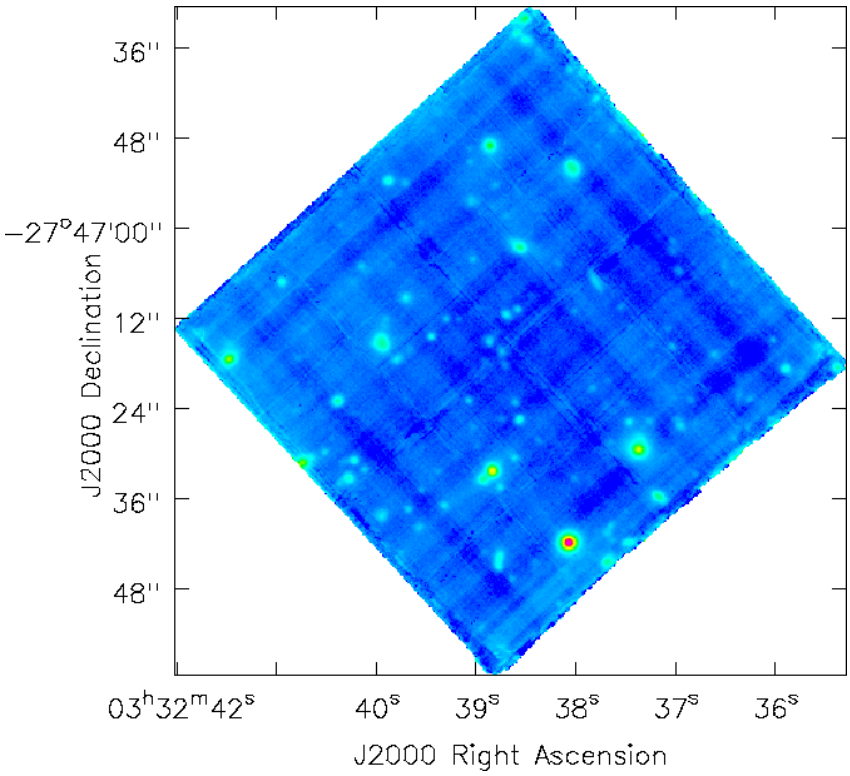

Figure 1: The reconstructed white-light image of all exposures combined

To combine the data of different exposures correctly, we had to determine the relative astrometric offsets first. The coordinates of bright sources are extracted from the white-light images, which are used to compute the relative astrometric offset of each dataset. The final white-light image produced in this step is shown in Figure 1.

3 Results

We detected objects on the white light image and the datacube by eye inspection. A total of 98 objects were obtained from the white light image and additionally 19 objects were found in the datacube only. We extracted the spectra from the datacube using a python program provided by W. Karman. The quality of the spectra suffered from skylines and additional non-object related flux at blue wavelengths. This additional flux varied across the datacube and was different for all datacubes of individual exposures, making it very hard to remove. Also visible in the images are vertical and horizontal bands (see the white-light image from Figure 1). They are intrinsic to the instrument and are caused by residuals from splitting the instrument channels (Bacon et al. 2015).

Therefore, we decided to create a new datacube with the median of the entire datacube removed. We preferred using the median over the mean to prevent real lines from being included in this spectrum and consequently removed. This median spectrum is shown in Figure 2. All lines present here are skylines. Also visible is the higher than average flux at blue wavelengths. Skylines however differ across the datacube, so they could not be removed from the object spectra in this way. We assessed objects on a case by case basis whether to use this new datacube or the old one for redshift determination.

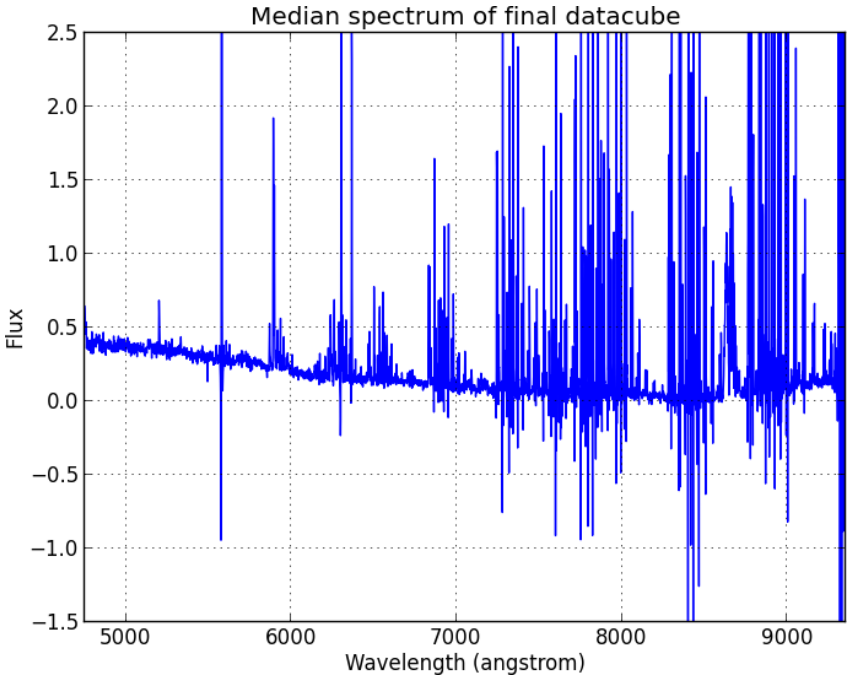

Figure 2: The median spectrum of the final datacube. Note the presence of multiple skylines towards the NIR regime.

Once the spectra were extracted, they were compared to line positions and shifted with another python program provided by W. Karman. The spectral line templates in this program were taken from the NIST Atomic Spectra Database. We used these line templates to determine the redshifts of sources detected in the datacube. We present these redshifts in Table 2 in the appendix. The table also lists the assigned quality flags. A quality flag is an integer which indicates how secure the determination of the redshift of a source is. The quality flags here mean: 1. Very secure, 2. Secure, 3. Insecure, 4. Very insecure, 9. One line fit. A redshift of -9.0 means that no redshift could be determined for the source. These objects have a quality flag of 0.

The RA and DEC given in Table 2 are based on the coordinates from the first exposure. By using the CASA viewer, we determined the astrometric shift from an F814W image of the HUDF. We used these corrected coordinates to cross correlate with the CANDELS GOODS-South catalog. Table 3 (in the appendix) shows the corrected coordinates and the separation in arcseconds between these coordinates and the coordinates from the CANDELS catalog. Notice that the only star in the field (MUSE ID 107, CANDELS ID 13473) shows a separation of 0.17 arcseconds. We cross correlated the data with a matching radius of 1". The cross correlation is secure in spite of the small astrometric shift.

In Table 3, the IDs given to the objects in the CANDELS catalog are shown in the column named ID2, while the IDs given to the objects in this thesis are shown in the column named ID. The data in the columns zspec_old, zphot and F606W are from CANDELS. The CANDELS cross correlation is further discussed in section 3.4.

3.1 Redshift distribution of MUSE sources

A stacked histogram of the redshift distribution of galaxies found by MUSE can be seen in Figure 3. We colored the bars in the histogram according to the quality flags of the determined redshifts. It appears that we tend to be more secure about objects with low redshift than objects with high redshift. We can easily explain this by the fact that low redshift objects are closer and therefore tend to have a higher apparent brightness than high redshift objects. This makes determining redshifts easier. After a redshift of about 1, the results are not so certain anymore.

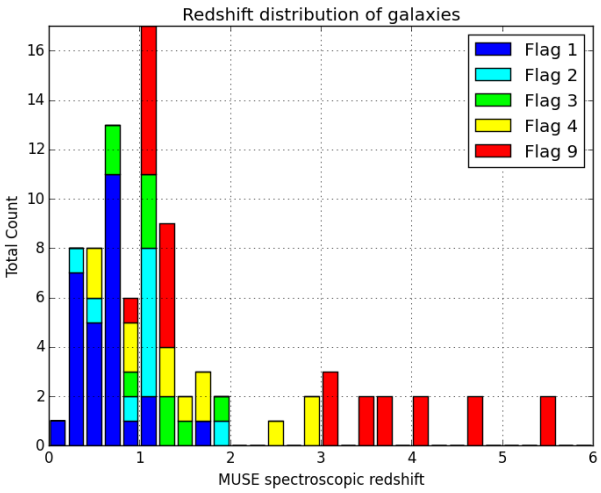

Figure 3: A stacked histogram of the redshifts of the objects found in the MUSE datacube, where the colors indicate the quality flags.

One may recognize the redshift desert in this plot, though more sources would have made this more apparent. Deeper imagery would mainly show more high redshift sources.

3.2 Individual sources found in the MUSE datacube

3.2.1 Low redshift objects (z<1)

We found 36 objects with z<1 in the FOV. Most of these objects have a quality flag of 1. They are closer and therefore generally apparently brighter than objects with higher redshifts, which makes their redshifts easier to determine.

Emission lines are indicators of star formation: gas ionized by young hot stars emit light by radiative recombination. We found prominent emission lines in the spectra of 19 objects with z<1. There are also 15 objects which show faint emission lines in their spectra. These objects have a lower star formation rate and consist mostly of older stars. If the continuum of these objects is visible, they show a high flux at red wavelengths.

There are 4 objects with z<1 whose spectra show prominent absorption lines. These objects contain mostly old stars which are not hot enough to ionize the surrounding interstellar medium. The emitted photons are absorbed by gas and dust (if present) (Draine 2011). Due to a lack of time we were not able to investigate the contribution of gas and dust to the spectra in detail.

Figures 4 and 5 show the spectrum of object 10, which is a source with bright emission lines. As with many low redshift objects with quality flag 1, the continuum is clearly visible. Balmer break absorption features can be seen too. The distinctive Hβ/OIII triplet is apparent in Figure 5. This is an intensively star forming galaxy.

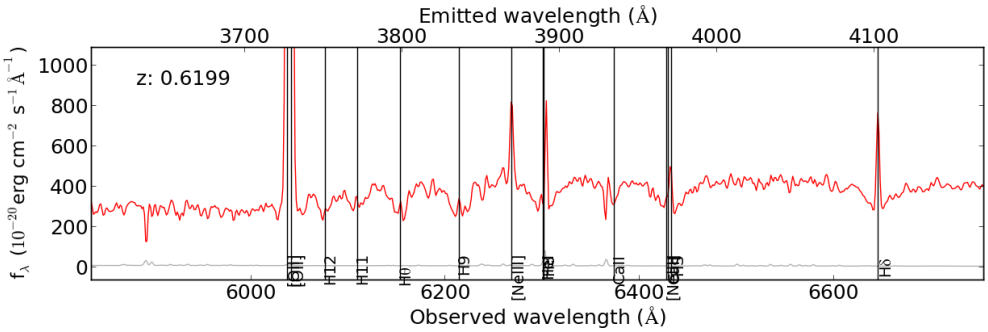

Figure 4: 1D spectrum of object 10 in the wavelength range from 5825Å to 6760Å.

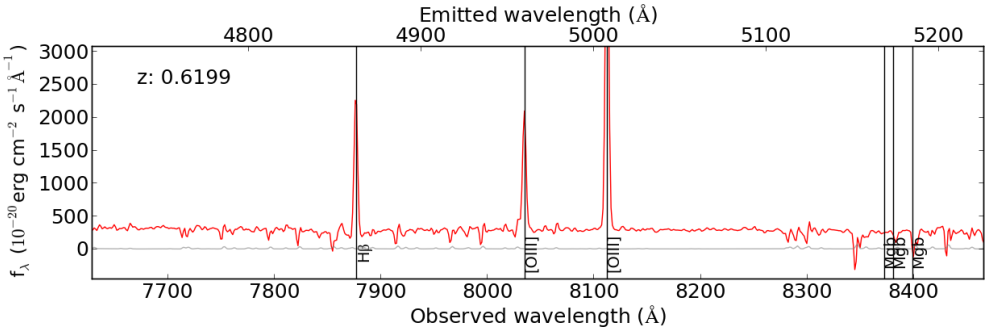

Figure 5: 1D spectrum of object 10 in the wavelength range from 7630Å to 8465Å.

The CaII and NeIII/CaII/Hε absorption features are clearly visible in the spectrum of Object 70. They are important features to look for in bright, low redshift objects. Additionally, a faint OII emission line can be seen in the spectrum of object 70. The spectrum of this galaxy is very red, so it contains mostly old stars. The faint OII line shows that some star formation is going on, so the galaxy can not be classified as passive. The absorption lines are however much more prominent.

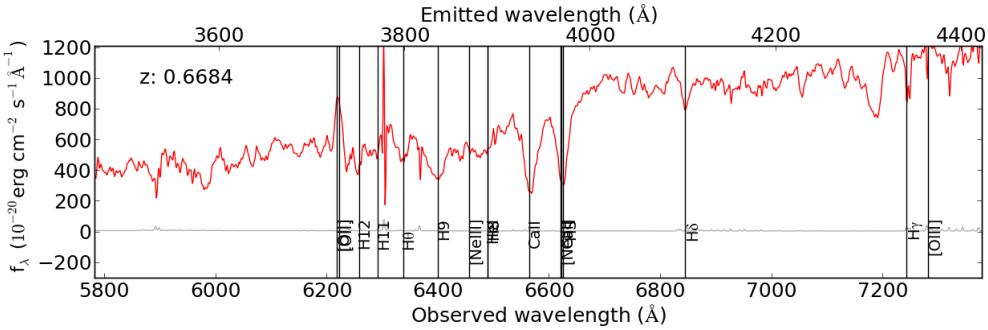

Figure 6: 1D spectrum of object 70.

A low redshift does not always imply that the redshift is easily determined from the spectra. An example of this can be seen in Figure 7, which shows the spectrum of object 76. This object is very faint despite its low redshift. Meticulous examination of the datacube revealed that one of the lines in between the skylines was in fact OII emission from this object.

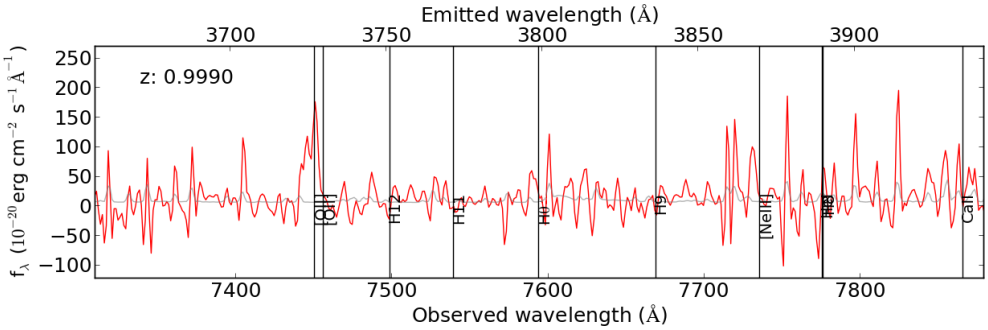

Figure 7: 1D spectrum of object 76.

3.2.2 Intermediate redshift objects (1<z<3)

In this redshift range we found 36 objects. These objects have mostly flags 2 and 3. Yet, bright objects still appear here. We found strong emission lines in 14 spectra and strong absorption lines in 4 spectra of objects with 1<z<3.

Object 35 displays prominent OII emission lines, indicating star formation. OII will shift out of the spectral range of MUSE for redshifts higher than 1.5. In general, no prominent emission lines are present between OII and Lyα. This means that between z=1.5 and z=2.9, very few objects can be spectroscopically determined. This redshift regime is called the 'redshift desert' (Bacon et al. 2015).

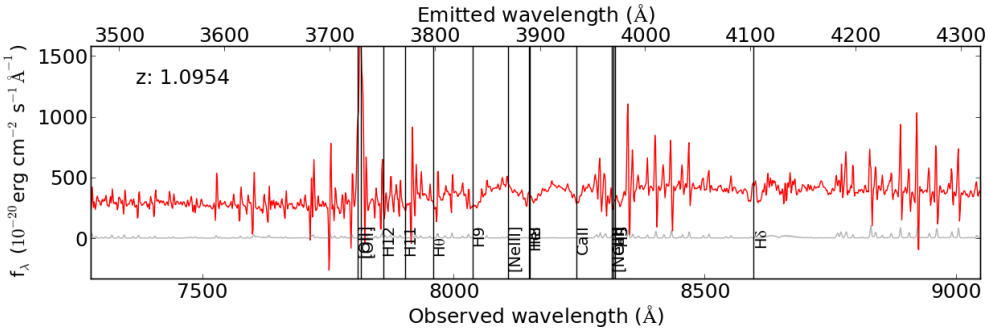

Figure 8: 1D spectrum of object 35.

Object 62 is an object for which no emission lines can be seen. At z=1.9060, it is in the 'redshift desert'. It is however bright enough for absorption lines to be visible.

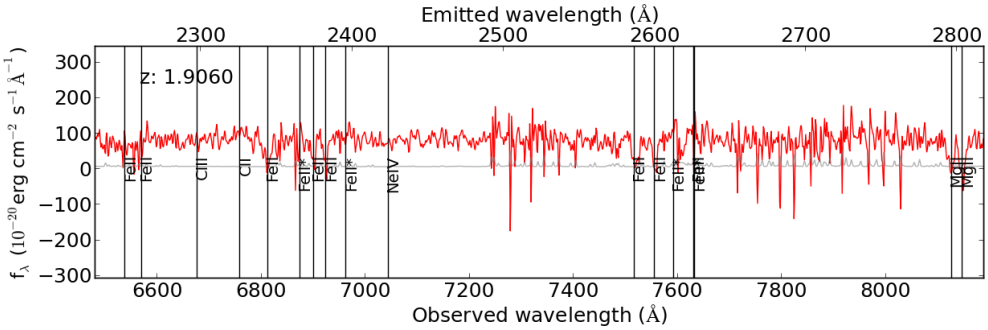

Figure 9: 1D spectrum of object 62.

There are also faint objects in the intermediate redshift region. Figure 10 shows a case where we are very uncertain about whether or not the continuum is visible. Some Fe absorption lines may be present in object 13, but this identification is very insecure. For 33 objects, we were not able to determine a redshift. We suspect these may be in the redshift desert as well.

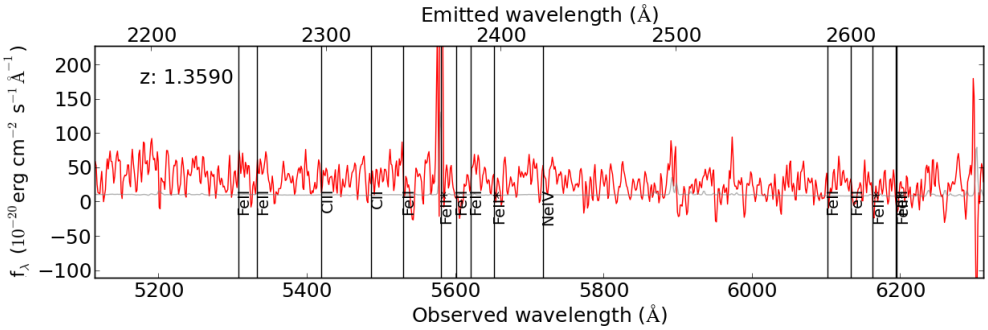

Figure 10: 1D spectrum of object 13.

3.2.3 High redshift objects (z>3)

We identified 12 objects with z>3. All of them have quality flag 9 and are Lyα emitters. No other emission lines are visible at z>2.9 and no object found was bright enough to show clear continuum beyond z=2. These

are the sort of objects MUSE can find much more easily than broad band photometric detectors, due to their low average flux in their passbands.

A very bright Lyα emitter is object 46, whose spectrum is shown in Figure 11. The characteristic red tail of Lyα is clearly visible. This is however not always the case. The red tail seen in the line profile is a result of resonant scattering of Lyα photons. The random motion of H atoms in the interstellar gas around hot stars causes Doppler shifts on scattered Lyα photons. The optical depth in HII regions becomes smaller for longer wavelengths, so Lyα photons which have Doppler shifted to slightly longer wavelengths have a larger probability of escaping the HII region and can consequently be detected on Earth. Hence the flux in the red wing of the profile is higher (Draine 2011; see also Zheng et al. 2010).

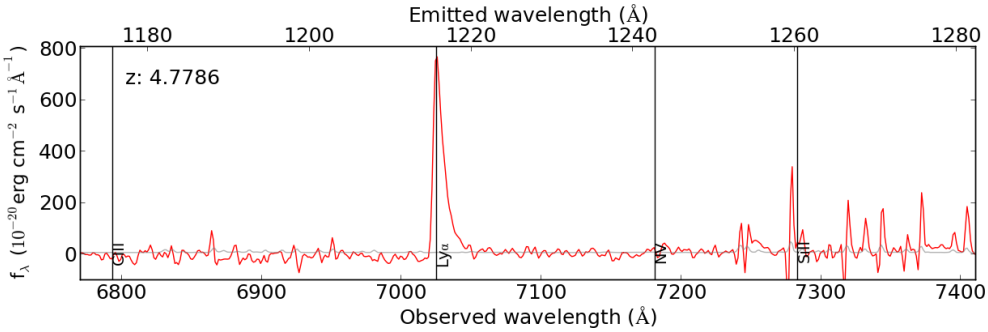

Figure 11: 1D spectrum of object 46.

An example of weak Lyα emission is shown in Figure 12. The line looks like Lyα, but due to its weakness the line profile is heavily influenced by the surrounding noise. This can lead to cases where the nature of the line is unclear. A special case is the group of sources consisting of the objects 30, 31 and 32, which we discuss in the next section.

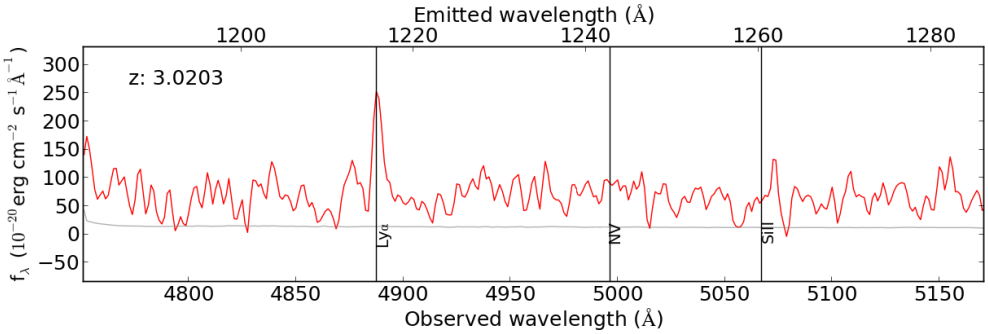

Figure 12: 1D spectrum of object 9.

3.2.4 A galaxy group candidate at high z

The objects 30, 31 and 32 all appear close to each other in the datacube. Their spectra show an emission line at the same observed wavelength. The nature of this line is however unclear. Candidates are Lyα and OII, which would significantly alter the redshift determination. If the lines are Lyα, the redshifts for objects 30, 31 and 32 would be 5.4722, 5.4730 and 5.4710. If they are OII, these would change to 1.1103, 1.1102 and 1.1101.

Meticulous examination of the datacube revealed the objects (see Figure 16). No doublet can be distinguished in the multiple skylines surrounding the emission line. Additionally, none of the characteristics of Lyα are visible.

If the line is indeed Lyα, then we would expect the objects to be absent in filters bluer than the observed wavelength of the Lyα line. We therefore looked at the brightness of the objects in the F435W filter. For the objects 30, 31 and 32, the F435W AB magnitudes are 37, 29 and 28, respectively. The limiting AB magnitude of the CANDELS survey is 28.4 in the optical (Koekemoer et al. 2011). We did not find the limiting magnitude in the F435W filter, but the value for the optical should give an indication. We therefore conclude that object

30 is not observed in this filter which means Lyα can not be excluded as a possibility. Object 32 should be a safe detection. We think that OII is a more likely identification of the emission line. Object 31 is a marginal detection. We can not conclude which identification is more likely for this object.

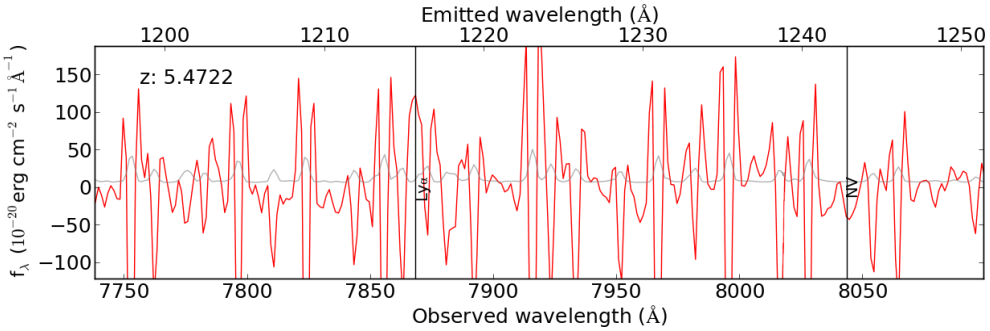

Figure 13: 1D spectrum of object 30

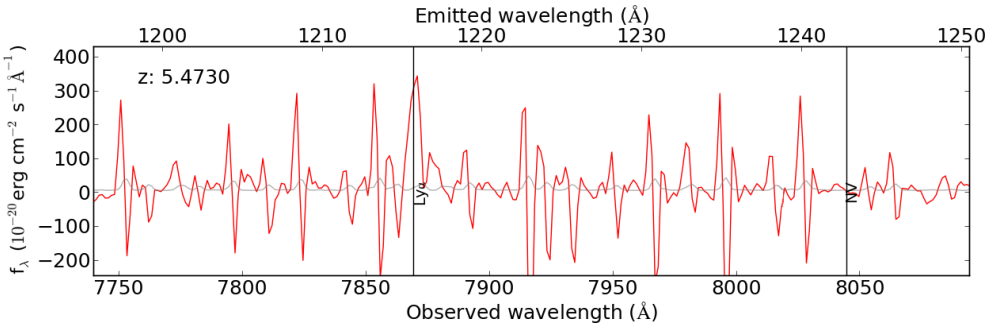

Figure 14: 1D spectrum of object 31

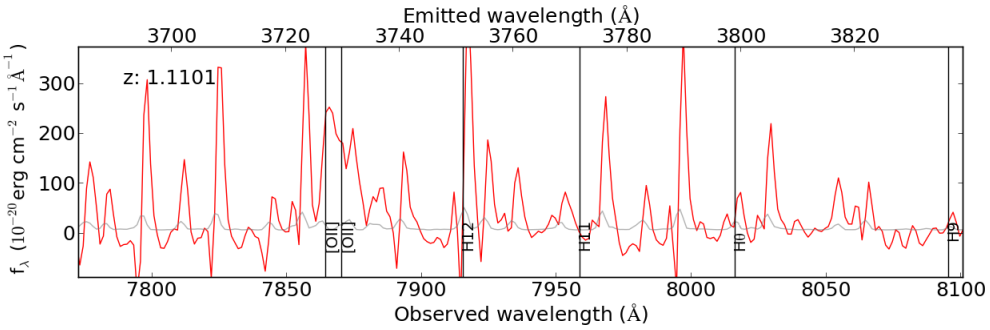

Figure 15: 1D spectrum of object 32

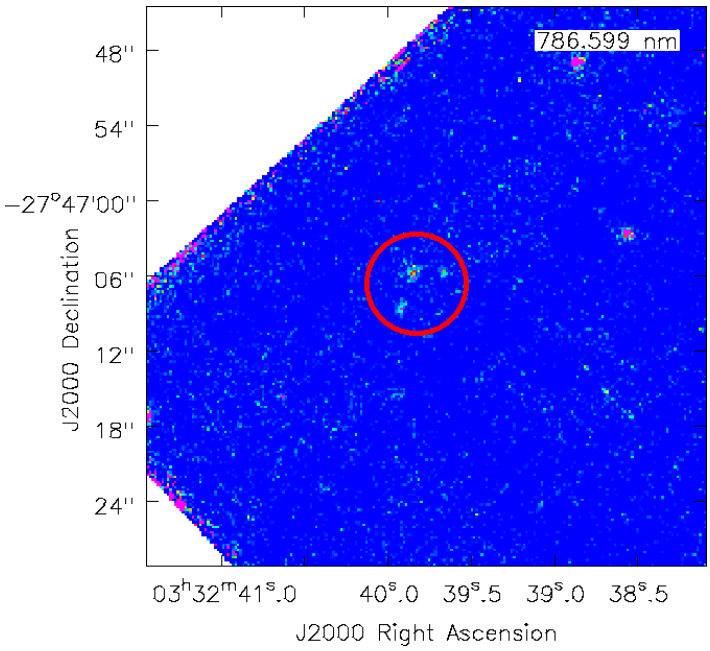

Figure 16: Emission from objects 30, 31 and 32 (red circle)

3.3 Star Formation Rates

Table 1: Star Formation Rates of objects with flag 1 and 2 in $M_{\odot} yr^{-1}$

ID	zspec	Hα SFR	OII SFR	ID	zspec	Hα SFR	OII SFR
10	0.6199	N/A	2.102±0.601	83	0.3235	0.013±0.001	0.015±0.005
11	0.6217	N/A	0.125±0.036	84	0.3375	0.023±0.002	0.058±0.017
12	0.7190	N/A	0.100±0.029	86	1.0957	N/A	2.752±0.787
14	1.0966	N/A	0.729±0.210	88	1.0365	N/A	1.412±0.404
20	0.9538	N/A	0.458±0.133	94	0.4585	N/A	0.740±0.211
24	0.2759	0.054±0.001	0.525	97	0.4582	N/A	1.861±0.532
26	0.6220	N/A	0.035±0.012	100	0.8327	N/A	0.131±0.039
28	0.6190	N/A	0.778±0.222	101	0.2318	0.125	N/A
35	1.0954	N/A	3.000±0.857	102	1.0958	N/A	2.652±0.759
38	1.0959	N/A	1.971±0.563	103	1.0945	N/A	1.027±0.294
39	0.4681	N/A	0.061±0.018	104	0.6642	N/A	0.217±0.062
42	0.6646	N/A	0.240±0.069	106	1.0984	N/A	2.116
45	0.9798	N/A	0.615±0.176	109	0.3104	0.033±0.001	0.056±0.016
61	0.6673	N/A	1.063	110	0.3103	0.023±0.001	0.043±0.012
64	0.2272	0.008	N/A	111	0.4314	N/A	0.039±0.012
65	0.4238	0.006±0.003	0.028±0.008	116	0.6644	N/A	0.036±0.012
70	0.6684	N/A	0.309±0.089	117	0.4235	-0.009±0.004	0.010±0.004
79	0.3829	0.017±0.001	0.017±0.005				

For objects of which the redshift determination was secure (quality flag 1 and 2), we calculated a lower limit of the Star Formation Rates (SFR) of these galaxies. They can be calculated from the luminosities of Hα and OII (Kennicutt 1998):

$$SFR(M_{\odot} yr^{-1}) = 7.9 \cdot 10^{-42} L(H\alpha)[ergs \cdot s^{-1}] \quad (1)$$

$$SFR(M_{\odot} yr^{-1}) = (1.4 \pm 0.4) \cdot 10^{-41} L(OII)[ergs \cdot s^{-1}] \quad (2)$$

The uncertainty given in equation 2 is due to the scaling factor depending on the type of galaxy. The lower limit represents blue emission-line galaxies while the upper limit represents luminous spiral and irregular galaxies (Kennicutt 1998).

To calculate the luminosity of the Hα and OII emission lines, we first shifted the spectra of the sources we wanted to calculate the SFR for to their emitted wavelength. This allowed us to compute the value of the continuum by taking the median of a small region around the emission line. We subtracted this value from the line region and integrated this region to obtain the total flux contained in the emission line. The luminosity of the lines can then be calculated with equation 3:

$$L = 4\pi {d_L}^2 f \tag{3}$$

where f is the integrated flux and d_L is the luminosity distance. We calculated the luminosity distance using Ned Wright's cosmology calculator (Wright 2006). Finally we applied equations 1 and 2 to calculate the values listed in Table 1. OII and Hα were not visible in all spectra. When they were not visible, we indicated this with 'N/A' in the table. For some objects, we were not able to calculate the uncertainties. Therefore they are not listed in the table for these objects.

The negative value of the SFR based on Hα of object 117 can be explained by looking at the spectrum. There are many skylines in the region where the Hα emission line is supposed to be. This will have influenced the determination of both the flux of the continuum and the integrated flux of the Hα line.

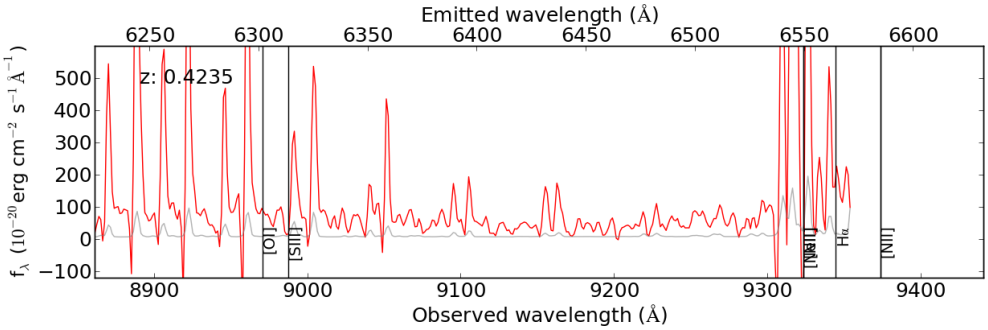

Figure 17: 1D spectrum of object 117

The other values found for the SFR are in the range 0.01 to $2.5 M_{\odot} yr^{-1}$. These are not corrected for any interstellar or intergalactic absorption, so they are lower limits. The Hα line is influenced more by dust absorption than the OII line, because its wavelength is longer. Besides object 117, there are some other objects where skylines likely influence the computation of the corresponding SFR. This is the case with OII for: 14, 20, 24, 35, 38, 102; and with Hα for: 65, 83, 84.

There are 12 galaxies with SFR<0.1, 13 with 0.1<SFR<1 and 10 with SFR>1. The SFR of those 10 galaxies are comparable to the Milky Way.

3.4 CANDELS cross-correlation

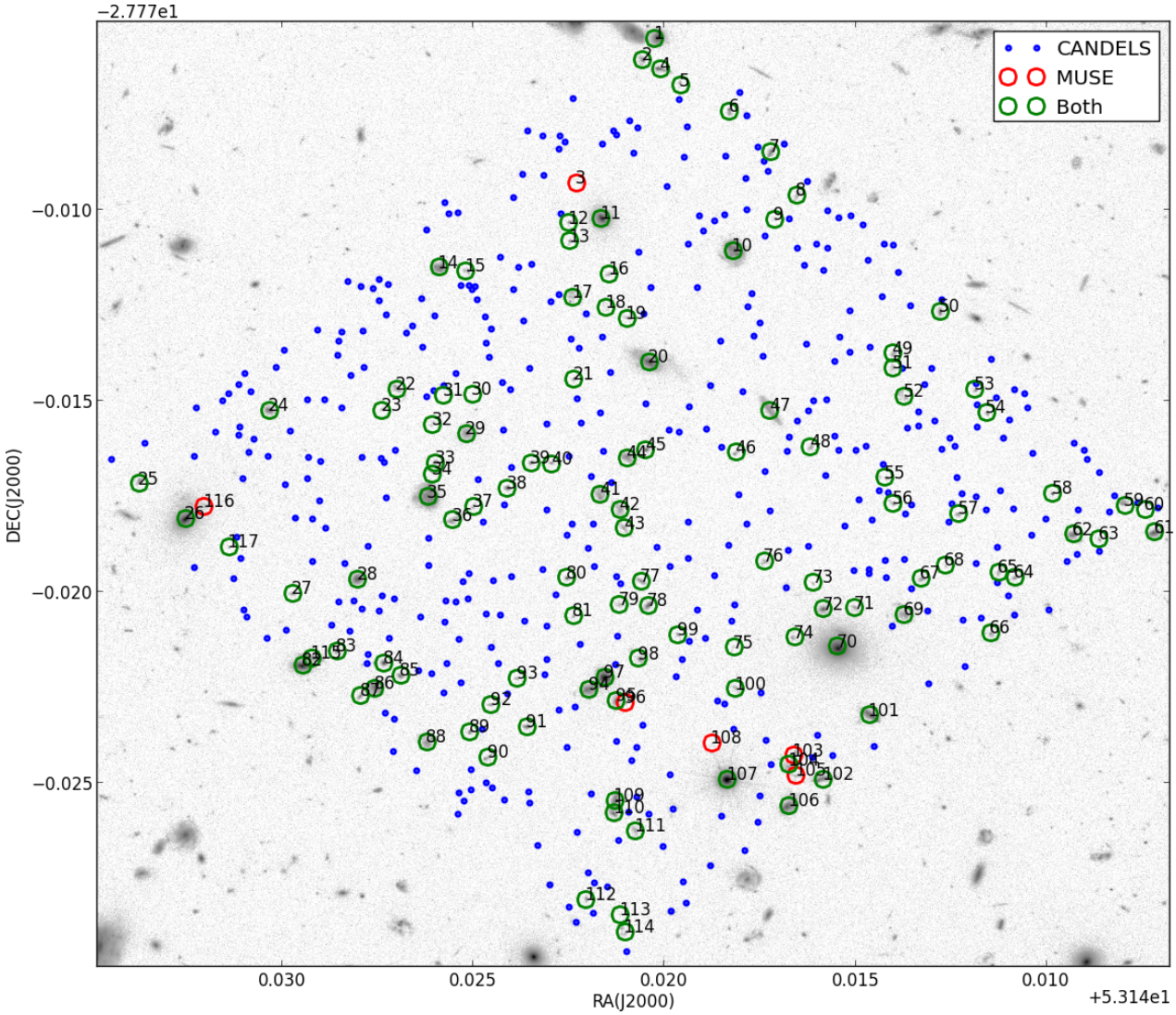

Figure 18: Location of all known objects in field of view of our MUSE pointing. Blue circles indicate the positions of objects in the CANDELS catalog which we did not see in our MUSE datacube. Green circles indicate the positions of objects found in the datacube which were also present in the CANDELS catalog. Some objects found in the MUSE data were not present in the CANDELS catalog, these are indicated with red circles and are discussed in section 3.5.

We compared our data with the CANDELS GOODS-South galaxy catalog. This is an H-band selected catalog of a large area which includes the HUDF, which in turn includes the field of view of our MUSE pointing. Many objects in the CANDELS catalog which are in the common area are not detected in our MUSE data. There are also 6 objects which are not included in the CANDELS catalog, but are visible in the data obtained by MUSE. To understand why this is, a number of plots were made (see Figures 19 to 23).

The redshifts obtained in this research are compared to photometric redshifts from the CANDELS catalog and previously determined spectroscopic redshifts (when available) (Dahlen et al. 2013). Of 20 objects, the redshift determination was secure and different from the CANDELS catalog. Discussing all of these objects is beyond the scope of this report. Comments on these objects' spectra can be found in Table 2.

Unfortunately for this research the CANDELS catalog was based on the HST F160W filter, which is outside the spectral range of MUSE. But the CANDELS survey is much deeper than the MUSE data.

The Figures 19 to 23 show how the redshifts found with MUSE data compare to (spectroscopic and photometric) redshifts as listed in the CANDELS catalog. Although most redshifts are similar, some redshifts are

very different. The numbers in the Figures refer to the objects' IDs from Table 2. In Table 3, the column ID2 gives the IDs from the CANDELS catalog, which we did not use here. The ID column shows the IDs we gave to the objects in this thesis and are used in these figures.

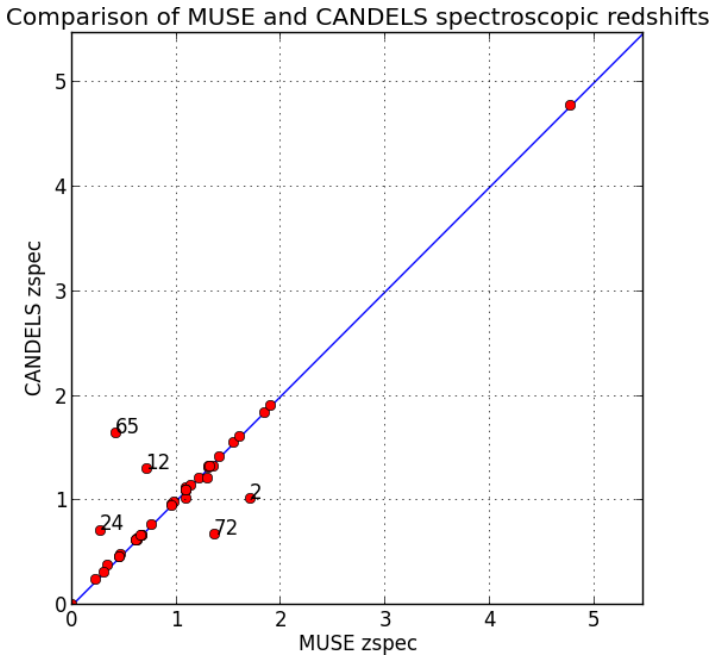

Figure 19: The old zspec listed in CANDELS compared to our new MUSE zspec

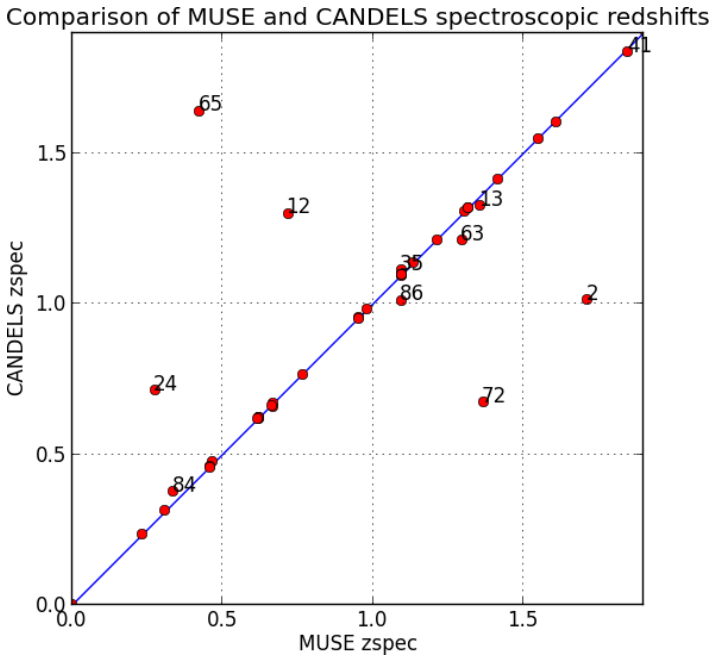

Figure 20: Zoom in on the region with many objects of Figure 19

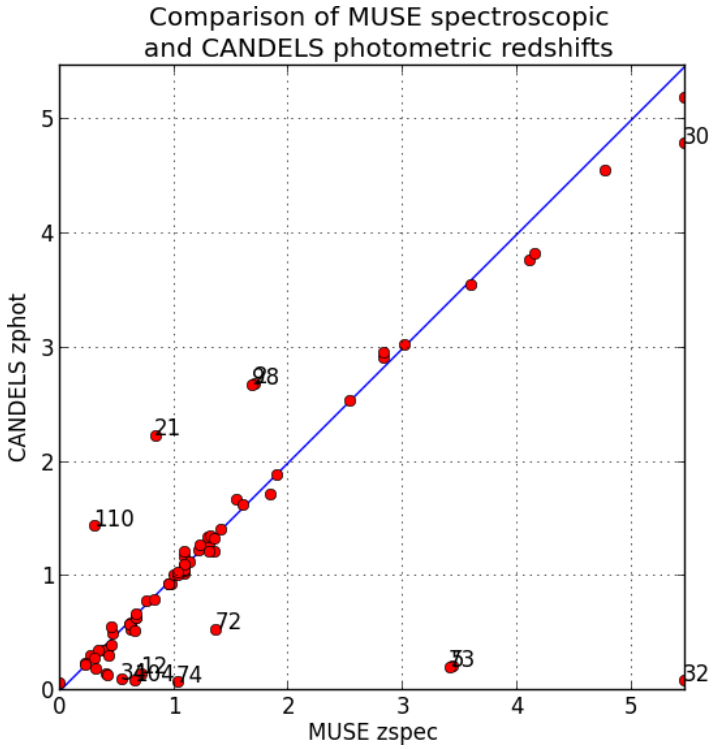

Figure 21: CANDELS zphot compared to our new MUSE zspec

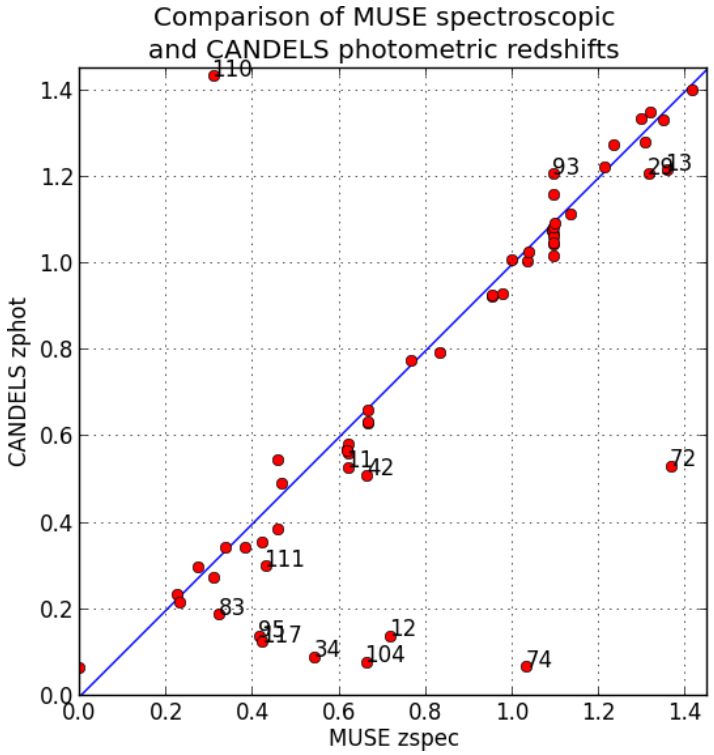

Figure 22: Zoom in on the region with many objects of Figure 21

Figure 23 shows up to what magnitude objects were found by MUSE and CANDELS. F606W is an optical filter for the HST WFC3, which has a spectral range which is near the center of the spectral range of MUSE (Guo et al. 2013). 'Continuum' here means that the objects were bright enough for the continuum to be visible in the spectrum. This was difficult to determine for faint objects. Emission lines are much easier to detect with

a spectrograph than with broad band photometry, hence objects detected solely by their emission lines are still detected at much fainter magnitudes.

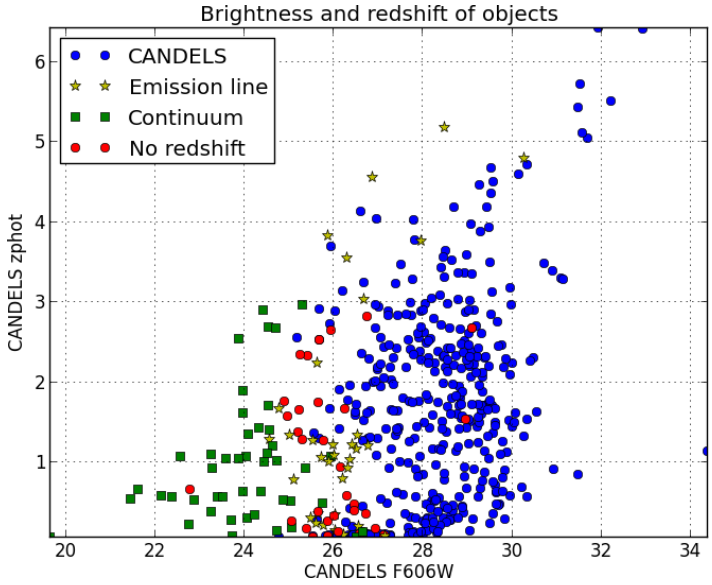

Figure 23: Photometric redshifts and F606W magnitude (both data from CANDELS) of all objects in the field of view present in CANDELS catalog. Blue dots represent objects not visible in the MUSE data.

There are 2 objects at F606W magnitude 29 for which we could not determine a redshift (objects 60 and 113). They are too faint for their continuum to be visible in the white-light image. Object 60 does not have an emission line in its spectrum. We therefore think it was mistaken for noise and that it was a coincidence that there was an object in the CANDELS catalog within the 1" matching radius. We did see an emission line in the spectrum of object 113, but we were unable to identify it.

We were also not able to determine a redshift for object 82, which, at roughly AB magnitude 22.5, is a bright object. There are clear absorption features and an emission line in the spectrum, but we could not find a matching line pattern in the line templates.

3.5 Objects detected in our MUSE data, but not present in CANDELS

The objects 3, 96, 103, 105, 108 and 116 were found in the data but they are not included in the CANDELS catalog. To prove their existence we added images of how they appear in the datacube.

Object 3 was found due to a weak emission line, which we identified as Lyα. This object may be too faint to be found by a broad band photometric survey like CANDELS. It is also difficult to distinguish from noise in the datacube. We decided it was an object due to its emission extending across multiple pixels in a circular pattern.

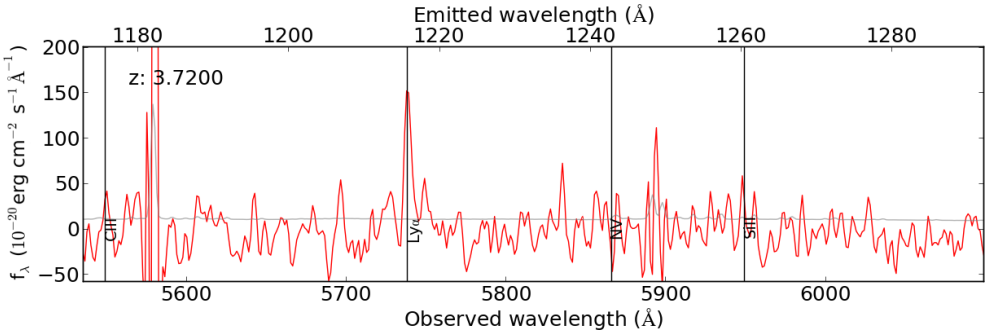

Figure 24: 1D spectrum of object 3

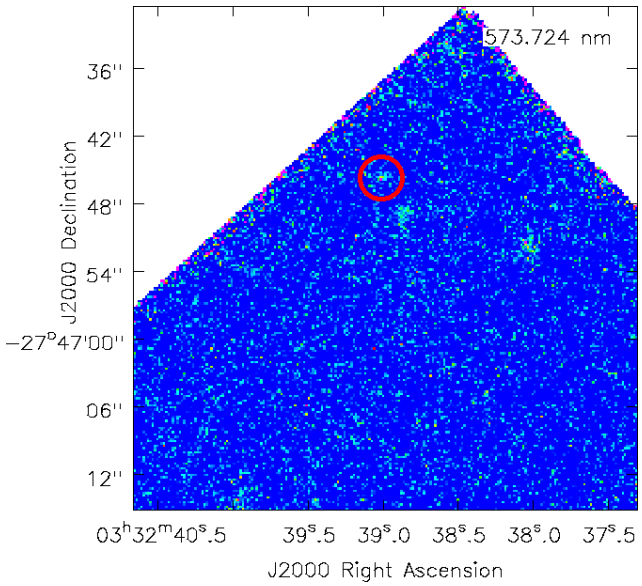

Figure 25: Emission from object 3 (red circle)

The same applies to object 96, though it is much brighter. Its proximity to object 95 may also cause source confusion.

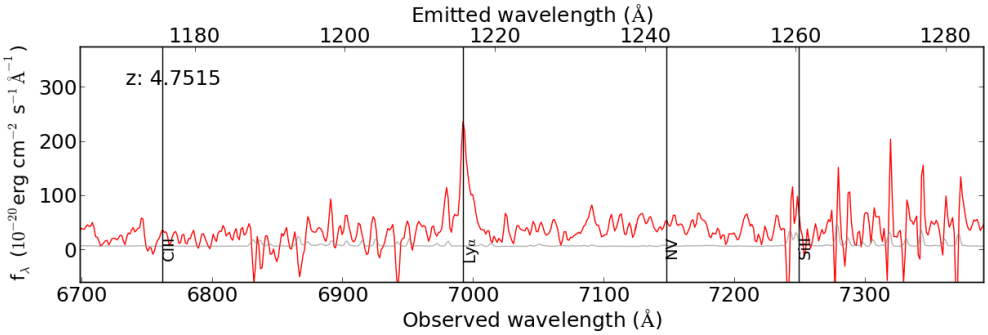

Figure 26: 1D spectrum of object 96

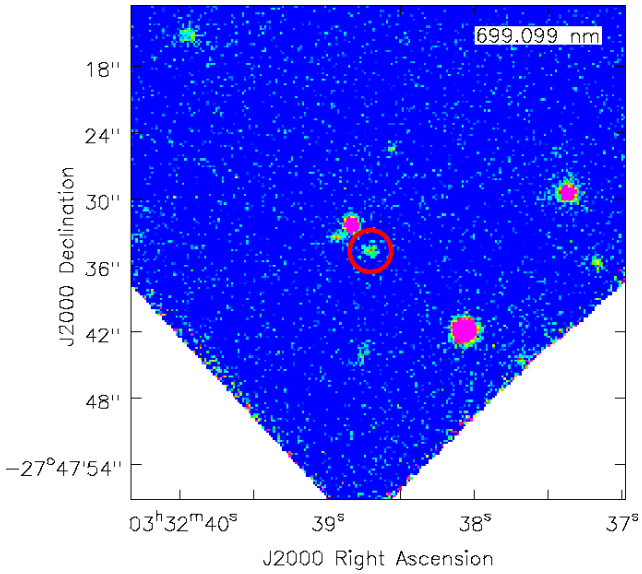

Figure 27: Emission from object 96 (red circle)

Object 108 may be blended with the nearby bright star (object 107). It is however also very faint, being only visible thanks to an emission line we identified as Lyα.

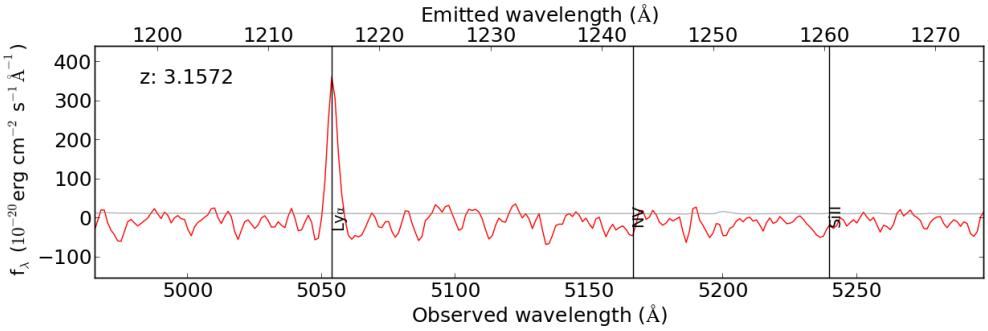

Figure 28: 1D spectrum of object 108

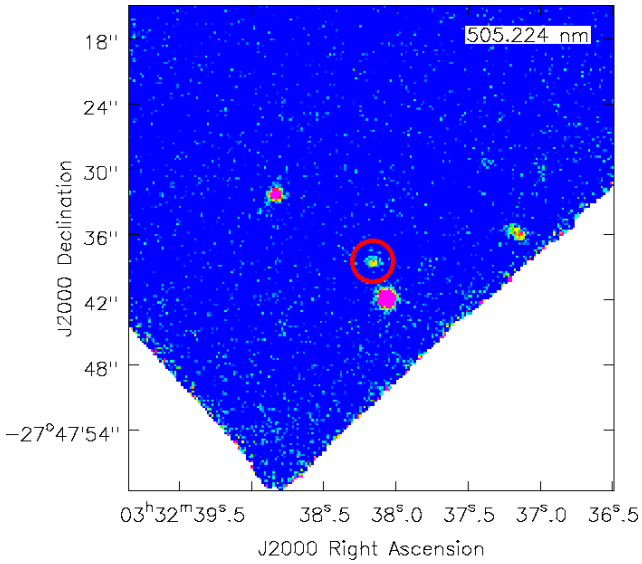

Figure 29: Emission from object 108 (red circle)

Object 116 is the third brightest of the objects not present in the CANDELS catalogue, showing the 3 Hβ and OIII lines in its spectrum. It may not have been catalogued due to its proximity to object 26. This object is very large and bright and might have overshone object 116 during the CANDELS survey. The outer regions of object 26 extend across object 116 which may have caused source confusion.

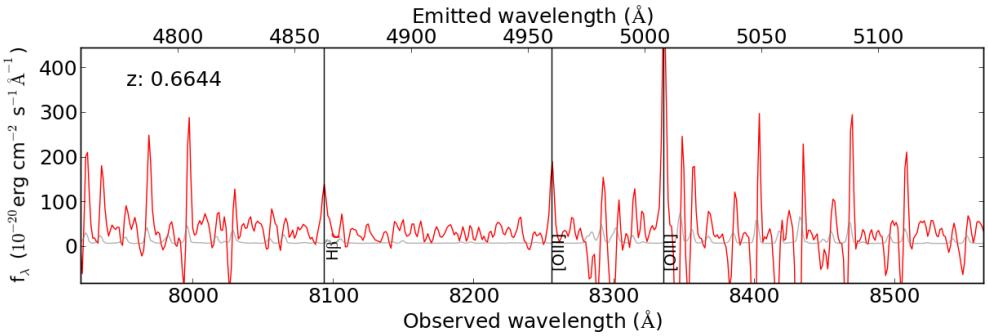

Figure 30: 1D spectrum of object 116

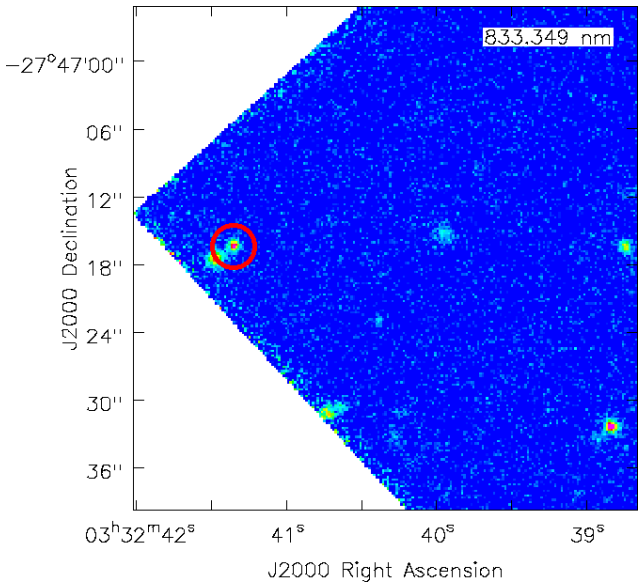

Figure 31: Emission from object 116 (red circle)

Objects 103 and 105 are large, relatively bright objects. These were not found by emission lines in the datacube, but were identified in the white-light image due to their high flux. A reason why these objects were not catalogued could be source confusion. They are located in a crowded region. The fact that the object in between (object 104) was catalogued seems to indicate that these three objects were considered as one. Proof of their independence is given by an HST image made in the F814W filter.

No redshift could be determined for object 105. Therefore, no fit to its spectrum can be shown.

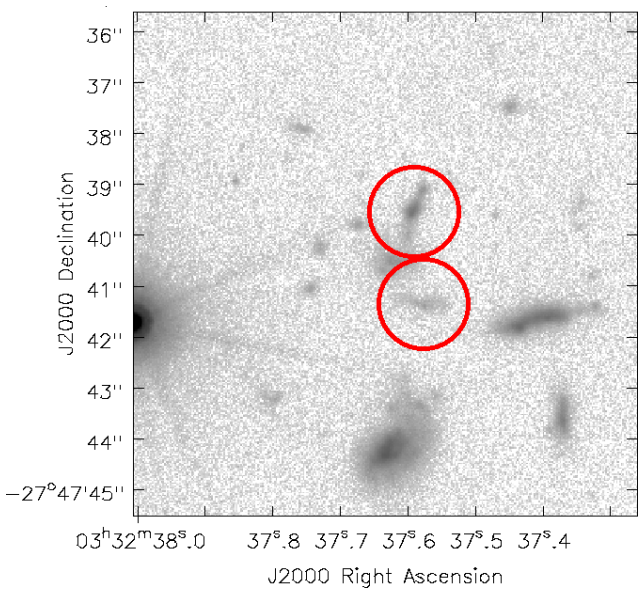

Figure 32: Zoom in on the region where objects 103 and 105 (red circles) reside

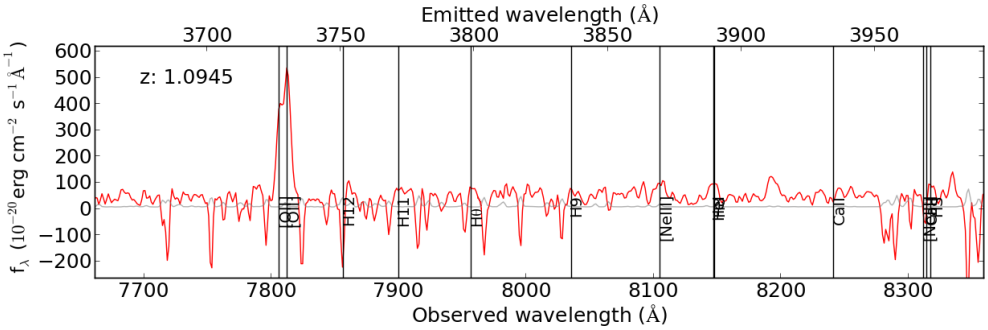

Figure 33: 1D spectrum of object 103

4 Discussion

With an exposure time of just under 6 hours, we have already found 117 objects in the 1 square arcminute field of view. The spectral resolution of the data is very good. For example, OII can clearly be distinguished as a doublet in the spectra obtained from the datacube.

Besides this MUSE is an excellent Lyα emitter detector. There is no need for knowing the location of objects beforehand, so MUSE can detect a lot of Lyα emitters in its FOV (provided their redshift is between 2.9 and 6.7) within just a few hours of exposure time. Other line emitters can also be found easily by MUSE.

The dataset used for this thesis was not very deep. Longer exposure times would have revealed more objects. Removal of atmospheric emission was not complete, though sufficient for this thesis' purpose.

Having a spectrograph like MUSE in space would remove the atmosphere completely. The lack of skylines and additional blue flux in such a case would make line identification much easier. Adaptive optics may also reduce these artifacts.

The use of adaptive optics starting this summer will improve the quality of the data. The resolution of the imagery without adaptive optics was not always sufficient to distinguish sources close to each other at the redshifts commonly encountered in the HUDF. But in general the spatial resolution of MUSE was good for this thesis' purpose.

The spectral range MUSE operates in poses some limitations to high redshift studies. The range is not wide enough to catch Lyα and OII in a single spectrum. This causes faint objects in the range of z=1.5 to z=2.9 to not be detected (the 'redshift desert').

The maximum wavelength of MUSE also limits the search for very high redshift galaxies (z>6). Extending the range further into infrared would aid in the quest for these objects and make OII visible again above a redshift of 1.5.

Finally the horizontal and vertical bands visible in the imagery are not beneficial to examining the data. They are not very prominent and of no importance when dealing with bright sources, but they impose difficulties on identifying the weakest sources MUSE can find.

5 Conclusion

The MUSE instrument has great potential in many fields of astronomy. Especially when adaptive optics becomes available. Its usefulness in high redshift studies mainly comes from its ability to detect line emitters whose average flux is too low to be detected with broad band photometry. Although many very faint line emitters were found in this research, none of them were completely absent from all HST images. Deeper MUSE data may reveal objects like this.

With almost 6 hours of total integrated exposure time, MUSE found 117 objects in the 1 square arcminute FOV. At z>1, a secure redshift determination was only possible for bright line emitters, which can still be seen clearly at higher redshifts.

The MUSE data contained 36 low redshift (z<1), 36 intermediate redshift (1<z<3) and 12 high redshift (z>3) objects. There are 19 star forming galaxies in the low redshift range and 14 in the intermediate redshift range.

The 13 objects with z>3 are all Lyα emitters. A candidate galaxy group was found at z=5.4, though the line identification remains uncertain.

We have calculated a lower limit for the SFR of 35 objects with a secure redshift determination. The SFR range from 0.01 to 3. For comparison, the Milky Way has a star formation rate of a few $M_{\odot} yr^{-1}$.

We found some disagreements when we compared the redshifts given in CANDELS catalog with those found with our MUSE data. For 20 objects, redshifts were different. Not all of these redshifts could be proven to be more correct than those from CANDELS, but for some new redshifts were determined.

Additionally we found 6 objects which are not present in the CANDELS GOODS-South catalog. We showed that reasons for this may be source confusion for 3 objects and too low average flux for the other 3 objects.

6 References

Bacon et al., 2014, The Messenger, 157, 13
Bacon et al., 2015, A&A, 575A, 75
Bouwens et al., 2004, ApJ, 611, 1
Bouwens et al., 2010, ApJ, 709, 133
Bunker et al., 2004, MNRAS, 355, 374
Contini et al., 2015, arXiv:1512.00246
Dahlen et al., 2013, ApJ, 775, 93
Draine, 2011, Physics of the Interstellar and Intergalactic Medium
Ellis et al., 2012, ApJ, 763, 7
Fosbury et al., 2001, The Messenger, 105, 40
Grogin et al., 2011, ApJS, 197, 35
Guo et al., 2013, ApJS, 207, 24
Karman et al., 2015, A&A, 574, 11
Kelz et al., 2015, arXiv:1512.03329
Kennicutt, 1998, ARA&A, 36, 189
Koekemoer et al., 2011, ApJS, 197, 36
MUSE Pipeline User Manual, 2016
NIST Atomic Spectra Database, 2016, `http://physics.nist.gov/PhysRefData/ASD/lines_form.html`
Wright, 2006, PASP, 118, 1711
Zheng et al., 2010, ApJ, 716, 574

7 Acknowledgments

My supervisors for my Bachelor thesis were Karina Caputi and Wouter Karman, both from the Kapteyn Astronomical Institute in Groningen.

Appendix

Table 2: Properties of all objects found by MUSE

ID	RA	DEC	zspec	flag	comments
1	53.160585	-27.775600	0.6230	3	Balmer break features barely visible
2	53.160777	-27.776109	1.7150	4	Seems like FeII 2382A absorption at 6446A
3	53.162546	-27.779372	3.7200	9	Very weak line at 5737A, guess LyA
4	53.160375	-27.776380	2.5428	4	Looks like CIV absorption at 5450A
5	53.159842	-27.776844	3.4389	9	LyA at 5395A
6	53.158544	-27.777487	1.5507	4	Fitted MgII emission at 7140A
7	53.157467	-27.778538	1.3066	9	Continuum is very faint if visible. OII doublet.

8	53.156796	-27.779661	-9.0	0	Looks like FeII 2374A absorption at 5035A, z=1.1140?
9	53.157375	-27.780312	3.0203	9	There could be a line at 4887A, fitted LyA.
10	53.158460	-27.781148	0.6199	1	Balmer break absorption and emission features clearly visible.
11	53.161915	-27.780300	0.6217	1	CaII and NeIII/CaII/Hε absorbtion clearly visible.
12	53.162760	-27.780434	0.7190	1	OIII/Hβ lines clearly visible.
13	53.162733	-27.780898	1.3590	4	FeII around 2600A and extremely weak CIII line present.
14	53.166142	-27.781574	1.0966	1	MgII absorption visible, Mg emission, OII line
15	53.165442	-27.781672	-9.0	0	
16	53.161688	-27.781744	-9.0	0	
17	53.162671	-27.782349	1.4153	3	Doublet at 9006A, first peak coincides with skyline.
18	53.161771	-27.782615	-9.0	0	
19	53.161219	-27.782912	-9.0	0	If CIV absorption at 4800A, z=2.0980.
20	53.160673	-27.784044	0.9538	2	Balmer break features visible but covered in noise.
21	53.162635	-27.784494	0.8429	3	Extremely weak line at 6893A, very noisy
22	53.167285	-27.784756	-9.0	0	
23	53.167656	-27.785342	-9.0	0	Absorption at 5425A.
24	53.170577	-27.785323	0.2759	1	OIII/Hβ lines clearly visible.
25	53.174004	-27.787309	-9.0	0	
26	53.172781	-27.788148	0.6220	1	CaII and NeIII/CaII/Hε absorbtion clearly visible.
27	53.169975	-27.790113	-9.0	0	Absorption at 4820A.
28	53.168271	-27.789739	0.6190	1	OII and OIII/Hβ lines clearly visible.
29	53.165429	-27.785927	1.3162	3	Balmer break features barely visible.
30	53.165279	-27.784914	5.4722	9	Very weak but broad line at 7866A.
31	53.166058	-27.784952	5.4730	9	Weak line at 7866A doesn't seem as broad as 30 and 32.
32	53.166333	-27.785703	1.1101	9	Weak but broad line at 7865A.
33	53.166231	-27.786698	-9.0	0	Absorption at 5600A.
34	53.166317	-27.787032	0.5440	4	Maybe OII at 5755A. OIII might be visible as well.
35	53.166433	-27.787588	1.0954	1	FeII lines and Balmer break features visible, Mg emission
36	53.165790	-27.788199	2.8410	4	Fitted OI and SiII at 5000A and 5860A.
37	53.165246	-27.787849	-9.0	0	
38	53.164348	-27.787359	1.0959	2	Very strong OII emission.
39	53.163733	-27.786698	0.4681	1	Clear OIII/Hβ emission.
40	53.163196	-27.786729	1.0963	9	OII doublet visible.
41	53.161938	-27.787554	1.8498	3	Fe absorption features around 6700A
42	53.161394	-27.787911	0.6646	1	OII doublet and OIII/Hβ visible
43	53.161271	-27.788417	1.0946	3	Fitted OII doublet at 7803A and 7810A.
44	53.161227	-27.786566	1.1349	3	OII doublet visible.
45	53.160725	-27.786340	0.9798	1	Strong OII emission.
46	53.158363	-27.786422	4.7786	9	Very bright assymetric line at 7022A.
47	53.157479	-27.785325	0.6671	3	Looks like OII at 6217A.
48	53.156419	-27.786259	0.9541	4	Fitted OII doublet at 7286A.
49	53.154273	-27.783798	-9.0	0	
50	53.153019	-27.782719	0.7660	1	OII doublet visible, OIII/Hβ in skyline region but visible.
51	53.154246	-27.784203	-9.0	0	
52	53.153981	-27.784926	-9.0	0	
53	53.152106	-27.784729	1.2153	9	Weak doublet at 8260A, fitted OII.
54	53.151823	-27.785352	3.6082	9	Line at 5600A, fitted LyA.
55	53.154463	-27.787071	-9.0	0	
56	53.154242	-27.787740	-9.0	0	
57	53.152546	-27.788020	-9.0	0	
58	53.150050	-27.787479	-9.0	0	
59	53.148125	-27.787892	-9.0	0	

60	53.147677	-27.787899	-9.0	0	
61	53.147377	-27.788483	0.6673	1	OII doublet and OIII/Hβ visible.
62	53.149542	-27.788545	1.9055	1	Many absorption features visible, like Fe.
63	53.148840	-27.788661	1.2980	9	Weak line at 8570A, fitted OII.
64	53.151071	-27.789681	0.2272	1	OIII/Hβ emission visible.
65	53.151485	-27.789557	0.4238	2	Weak OIII line at 7128A, OII doublet at 5310A.
66	53.151713	-27.791120	-9.0	0	
67	53.153535	-27.789696	-9.0	0	
68	53.152888	-27.789337	4.1183	9	Line at 6221A, guessed LyA, could be anything.
69	53.153948	-27.790669	1.3190	3	Bright doublet at 8641A, fitted OII.
70	53.155721	-27.791443	0.6684	1	CaII and NeIII/CaII/Hε absorbtion clearly visible.
71	53.155248	-27.790498	-9.0	0	
72	53.156075	-27.790506	1.3683	4	Absorbtion at 6630A might be MgII.
73	53.156321	-27.789791	3.4156	9	Assymetric line at 5366A, probably LyA.
74	53.156781	-27.791246	1.0336	3	Weak doublet at 7582A, fitted OII.
75	53.158388	-27.791487	4.1562	9	Assymetric line at 6266A, likely LyA.
76	53.157631	-27.789249	0.9990	9	Weak doublet at 7443A, fitted OII.
77	53.160858	-27.789771	1.0957	9	Line at 7815A, OII doublet.
78	53.160663	-27.790409	1.6102	2	Many absorption features and very faint CIII 1909 emission.
79	53.161429	-27.790424	0.3829	1	Line at 9076A, fitted Halpha.
80	53.162808	-27.789692	-9.0	0	
81	53.162621	-27.790687	-9.0	0	
82	53.169696	-27.791992	-9.0	0	Lines at 5288A and 6627A, spectrum contaminated by 115.
83	53.168817	-27.791634	0.3235	2	Faint OII and OIII/Hβ emission visible.
84	53.167585	-27.791945	0.3375	1	OII and OIII/Hβ emission visible.
85	53.167146	-27.792256	-9.0	0	
86	53.167815	-27.792606	1.0957	1	Very strong OII emission.
87	53.168192	-27.792778	2.8440	4	OI absorption at 5000A, CII at 5130A. Contaminated by 86.
88	53.166450	-27.793999	1.0365	2	OII doublet visible, quite noisy.
89	53.165335	-27.793734	-9.0	0	
90	53.164877	-27.794411	-9.0	0	Emission around 4850A? Not visible in datacube.
91	53.163840	-27.793610	1.3517	9	Line at 8771A, fitted OII.
92	53.164779	-27.793034	1.0953	9	Line at 7813A, OII doublet.
93	53.164102	-27.792326	1.0956	9	Line at 7815A, likely the same line as 92 (OII).
94	53.162196	-27.792632	0.4585	1	Very strong OIII/Hβ lines.
95	53.161498	-27.792909	0.4158	4	Contaminated by 94 and 97, OIII at 7083A, HeII at 6620A.
96	53.161254	-27.792962	4.7515	9	Weak line at 6991A, looks like LyA.
97	53.161790	-27.792301	0.4582	1	Very strong OIII/Hβ lines, nearby 94, but distinct.
98	53.160925	-27.791828	1.6878	4	Fe absorbtion lines.
99	53.159888	-27.791174	-9.0	0	Extremely weak lines at 5360A, 5386A and 5678A.
100	53.158392	-27.792590	0.8327	4	Weak line at 9175A, could be OIII.
101	53.154852	-27.793288	0.2318	1	Very strong OIII/Hβ lines.
102	53.156054	-27.794986	1.0958	2	OII doublet visible though quite noisy.
103	53.156854	-27.794356	1.0945	2	Balmer break features visible, quite noisy.
104	53.157013	-27.794613	0.6642	1	OII and OIII/Hβ lines visible.
105	53.156792	-27.794862	-9.0	0	Line at 6200A not part of 105 but of nearby 104.
106	53.156958	-27.795686	1.0984	2	Balmer break features visible, quite noisy.
107	53.158560	-27.794966	0.0004	1	A K3 type star. Continuum brighter than most skylines.
108	53.158998	-27.794022	3.1572	9	Line at 5052A, LyA.
109	53.161517	-27.795517	0.3104	1	OII and OIII/Hβ emission clearly visible.
110	53.161533	-27.795843	0.3103	1	Possibly merging with 109.
111	53.160988	-27.796326	0.4314	1	OII and OIII/Hβ emission faint but clear.

112	53.162281	-27.798130	1.0390	9	Line at 7593A, fitted OII.
113	53.161400	-27.798542	-9.0	0	Very weak line at 5072A, absorption at 5380A.
114	53.161213	-27.799008	1.2341	9	Weak line at 8331A, looks like doublet, guessed OII.
115	53.169479	-27.791800	-9.0	0	Line at 6205A, line at 8330A.
116	53.172288	-27.787838	0.6644	1	OIII/Hβ faint but clear.
117	53.171650	-27.788906	0.4235	1	OIII/Hβ faint but clear.

Table 3: All objects found matching with objects from the CANDELS GOODS-South catalog

ID	RA	DEC	zspec	flag	ID2	zspec_old	zphot	F606W	Separation
1	53.160335	-27.775535	0.6230	3	16035	0.6219	0.560	23.399	0.56
2	53.160527	-27.776045	1.7150	4	15876	1.0120	2.682	24.540	0.37
4	53.160125	-27.776316	2.5428	4	15798	-9.0	2.536	23.881	0.21
5	53.159592	-27.776780	3.4389	9	15718	-9.0	0.203	25.769	0.21
6	53.158294	-27.777423	1.5507	4	15591	1.5470	1.667	24.782	0.10
7	53.157217	-27.778473	1.3066	9	15501	1.3070	1.277	24.564	0.18
8	53.156546	-27.779596	-9.0	0	15316	1.3000	1.262	25.787	0.25
9	53.157125	-27.780248	3.0203	9	15097	-9.0	3.027	26.688	0.14
10	53.158210	-27.781084	0.6199	1	15282	0.6200	0.567	22.385	0.14
11	53.161665	-27.780235	0.6217	1	15782	0.6194	0.527	22.877	0.12
12	53.162510	-27.780370	0.7190	1	15162	1.2990	0.137	26.036	0.14
13	53.162483	-27.780834	1.3590	4	15099	1.3250	1.213	25.991	0.10
14	53.165892	-27.781510	1.0966	1	15122	1.0920	1.071	24.052	0.10
15	53.165192	-27.781607	-9.0	0	14975	-9.0	0.173	25.399	0.06
16	53.161438	-27.781679	-9.0	0	14947	-9.0	2.648	25.936	0.10
17	53.162421	-27.782285	1.4153	3	14946	1.4150	1.400	24.577	0.22
18	53.161521	-27.782550	-9.0	0	14763	-9.0	0.083	27.134	0.15
19	53.160969	-27.782847	-9.0	0	14688	-9.0	0.108	26.577	0.03
20	53.160423	-27.783979	0.9538	2	15040	0.9540	0.920	23.290	0.27
21	53.162385	-27.784429	0.8429	3	14451	-9.0	2.229	25.638	0.14
22	53.167035	-27.784691	-9.0	0	14533	-9.0	1.570	24.971	0.22
23	53.167406	-27.785277	-9.0	0	14285	-9.0	0.167	26.954	0.18
24	53.170327	-27.785259	0.2759	1	14437	0.7122	0.295	24.059	0.02
25	53.173754	-27.787245	-9.0	0	14191	1.6470	1.374	25.216	0.49
26	53.172531	-27.788084	0.6220	1	15156	0.6220	0.579	22.156	0.09
27	53.169725	-27.790048	-9.0	0	13556	-9.0	0.360	26.737	0.05
28	53.168021	-27.789675	0.6190	1	13781	0.6190	0.565	23.521	0.02
29	53.165179	-27.785863	1.3162	3	14839	1.3170	1.205	24.650	0.05
30	53.165029	-27.784850	5.4722	9	31206	-9.0	4.787	30.258	0.10
31	53.165808	-27.784887	5.4730	9	14349	-9.0	5.183	28.487	0.31
32	53.166083	-27.785639	1.1101	9	14291	-9.0	0.079	27.161	0.15
33	53.165981	-27.786633	-9.0	0	14133	-9.0	0.943	26.155	0.02
34	53.166067	-27.786968	0.5440	4	14018	-9.0	0.088	26.237	0.34
35	53.166183	-27.787524	1.0954	1	14520	1.1120	1.067	22.578	0.04
36	53.165540	-27.788134	2.8410	4	13975	-9.0	2.903	24.425	0.03
37	53.164996	-27.787784	-9.0	0	13965	-9.0	0.129	26.107	0.02
38	53.164098	-27.787295	1.0959	2	13995	1.0950	1.014	24.727	0.01
39	53.163483	-27.786633	0.4681	1	14074	0.4750	0.488	25.762	0.04

40	53.162946	-27.786664	1.0963	9	14046	1.0980	1.158	26.527	0.09
41	53.161688	-27.787489	1.8498	3	14263	1.8361	1.711	24.535	0.23
42	53.161144	-27.787847	0.6646	1	14057	-9.0	0.509	25.038	0.07
43	53.161021	-27.788353	1.0946	3	13890	-9.0	1.075	25.943	0.12
44	53.160977	-27.786501	1.1349	3	14267	1.1350	1.112	24.525	0.07
45	53.160475	-27.786276	0.9798	1	14194	0.9800	0.928	25.384	0.08
46	53.158113	-27.786358	4.7786	9	14141	4.7750	4.553	26.881	0.03
47	53.157229	-27.785261	0.6671	3	14629	-9.0	0.629	24.375	0.01
48	53.156169	-27.786194	0.9541	4	14162	0.9500	0.925	26.319	0.15
49	53.154023	-27.783734	-9.0	0	14591	-9.0	0.479	26.474	0.26
50	53.152769	-27.782655	0.7660	1	14898	0.7650	0.774	25.118	0.15
51	53.153996	-27.784138	-9.0	0	14549	-9.0	0.261	25.880	0.09
52	53.153731	-27.784862	-9.0	0	14415	-9.0	2.528	25.688	0.27
53	53.151856	-27.784665	1.2153	9	14383	1.2120	1.221	26.420	0.30
54	53.151573	-27.785287	3.6082	9	14278	-9.0	3.541	26.296	0.21
55	53.154213	-27.787007	-9.0	0	13982	-9.0	1.669	26.263	0.10
56	53.153992	-27.787676	-9.0	0	13893	1.7750	1.743	25.657	0.13
57	53.152296	-27.787956	-9.0	0	13854	-9.0	2.326	25.424	0.09
58	53.149800	-27.787415	-9.0	0	13920	-9.0	0.079	25.884	0.18
59	53.147875	-27.787827	-9.0	0	14040	1.8827	1.759	24.911	0.62
60	53.147427	-27.787835	-9.0	0	13829	-9.0	1.528	28.960	0.15
61	53.147127	-27.788418	0.6673	1	13911	0.6580	0.632	23.974	0.27
62	53.149292	-27.788481	1.9055	1	14042	1.9057	1.884	23.967	0.16
63	53.148590	-27.788596	1.2980	9	13758	1.2100	1.333	26.542	0.19
64	53.150821	-27.789617	0.2272	1	13589	-9.0	0.232	25.610	0.08
65	53.151235	-27.789492	0.4238	2	13681	1.6390	0.352	25.668	0.03
66	53.151463	-27.791056	-9.0	0	13516	-9.0	1.285	25.308	0.17
67	53.153285	-27.789632	-9.0	0	13730	-9.0	0.577	26.310	0.16
68	53.152638	-27.789273	4.1183	9	13570	-9.0	3.763	27.965	0.26
69	53.153698	-27.790604	1.3190	3	13689	1.3180	1.347	24.096	0.11
70	53.155471	-27.791378	0.6684	1	14608	0.6670	0.658	21.615	0.42
71	53.154998	-27.790433	-9.0	0	13530	-9.0	0.065	25.530	0.05
72	53.155825	-27.790441	1.3683	4	13678	0.6710	0.529	24.887	0.11
73	53.156071	-27.789726	3.4156	9	13597	-9.0	0.194	26.571	0.27
74	53.156531	-27.791182	1.0336	3	13357	-9.0	0.066	26.516	0.31
75	53.158138	-27.791423	4.1562	9	13330	-9.0	3.819	25.877	0.35
76	53.157381	-27.789185	0.9990	9	13682	-9.0	1.006	25.910	0.11
77	53.160608	-27.789706	1.0957	9	13657	1.0960	1.059	25.729	0.13
78	53.160413	-27.790344	1.6102	2	13552	1.6040	1.618	23.982	0.09
79	53.161179	-27.790360	0.3829	1	13487	-9.0	0.341	26.038	0.12
80	53.162558	-27.789627	-9.0	0	13618	-9.0	0.324	26.010	0.11
81	53.162371	-27.790623	-9.0	0	13422	-9.0	2.820	26.751	0.11
82	53.169446	-27.791927	-9.0	0	13661	0.6670	0.652	22.798	0.09
83	53.168567	-27.791569	0.3235	2	13511	-9.0	0.186	25.076	0.07
84	53.167335	-27.791881	0.3375	1	13374	0.3750	0.340	24.227	0.06
85	53.166896	-27.792192	-9.0	0	13382	-9.0	0.380	25.671	0.03
86	53.167565	-27.792542	1.0957	1	13400	1.0100	1.043	23.600	0.11
87	53.167942	-27.792713	2.8440	4	13183	-9.0	2.958	25.294	0.05
88	53.166200	-27.793934	1.0365	2	13086	-9.0	1.004	24.438	0.04
89	53.165085	-27.793660	-9.0	0	13066	-9.0	2.341	25.251	0.07
90	53.164627	-27.794347	-9.0	0	12950	-9.0	1.651	25.233	0.16
91	53.163590	-27.793546	1.3517	9	13081	-9.0	1.328	25.021	0.05

92	53.164529	-27.792970	1.0953	9	13120	-9.0	1.080	26.008	0.05
93	53.163852	-27.792262	1.0956	9	13212	-9.0	1.204	26.782	0.06
94	53.161946	-27.792568	0.4585	1	13292	0.4580	0.383	23.260	0.08
95	53.161248	-27.792844	0.4158	4	13485	-9.0	0.135	24.733	0.07
97	53.161540	-27.792237	0.4582	1	13526	0.4560	0.545	21.466	0.12
98	53.160675	-27.791763	1.6878	4	13414	-9.0	2.671	24.703	0.10
99	53.159638	-27.791110	-9.0	0	13385	-9.0	0.395	26.458	0.11
100	53.158142	-27.792526	0.8327	4	13274	-9.0	0.790	26.211	0.17
101	53.154602	-27.793224	0.2318	1	13392	0.2340	0.215	22.771	0.14
102	53.155804	-27.794922	1.0958	2	12997	1.0982	1.045	23.879	0.20
104	53.156763	-27.794548	0.6642	1	13281	0.6630	0.076	23.746	0.28
106	53.156708	-27.795622	1.0984	2	13097	1.0970	1.091	23.267	0.18
107	53.158310	-27.794902	0.0004	1	13473	0.0000	0.062	19.651	0.17
109	53.161267	-27.795452	0.3104	1	12904	0.3112	0.271	23.724	0.14
110	53.161283	-27.795779	0.3103	1	12880	-9.0	1.431	24.342	0.16
111	53.160738	-27.796261	0.4314	1	12706	-9.0	0.298	25.494	0.08
112	53.162031	-27.798066	1.0390	9	12438	-9.0	1.024	26.378	0.07
113	53.161150	-27.798477	-9.0	0	30709	-9.0	2.668	29.110	0.20
114	53.160963	-27.798944	1.2341	9	12350	-9.0	1.271	25.546	0.42
115	53.169229	-27.791736	-9.0	0	13265	-9.0	0.258	25.077	0.05
117	53.171400	-27.788841	0.4235	1	13792	-9.0	0.123	26.667	0.08